# Weak cubic $CaSiO_3$ perovskite in the Earth's mantle

https://doi.org/10.1038/s41586-021-04378-2

Received: 4 February 2021

Accepted: 22 December 2021

Published online: 9 March 2022

Check for updates

J. Immoor[1], L. Miyagi[2], H.-P. Liermann[3], S. Speziale[4], K. Schulze[5], J. Buchen[6], A. Kurnosov[1] & H. Marquardt[7]✉

Cubic $CaSiO_3$ perovskite is a major phase in subducted oceanic crust, where it forms at a depth of about 550 kilometres from majoritic garnet[1,2,28]. However, its rheological properties at temperatures and pressures typical of the lower mantle are poorly known. Here we measured the plastic strength of cubic $CaSiO_3$ perovskite at pressure and temperature conditions typical for a subducting slab up to a depth of about 1,200 kilometres. In contrast to tetragonal $CaSiO_3$, previously investigated at room temperature[3,4], we find that cubic $CaSiO_3$ perovskite is a comparably weak phase at the temperatures of the lower mantle. We find that its strength and viscosity are substantially lower than that of bridgmanite and ferropericlase, possibly making cubic $CaSiO_3$ perovskite the weakest lower-mantle phase. Our findings suggest that cubic $CaSiO_3$ perovskite governs the dynamics of subducting slabs. Weak $CaSiO_3$ perovskite further provides a mechanism to separate subducted oceanic crust from the underlying mantle. Depending on the depth of the separation, basaltic crust could accumulate at the boundary between the upper and lower mantle, where cubic $CaSiO_3$ perovskite may contribute to the seismically observed regions of low shear-wave velocities in the uppermost lower mantle[5,6], or sink to the core–mantle boundary and explain the seismic anomalies associated with large low-shear-velocity provinces beneath Africa and the Pacific[7–9].

$CaSiO_3$ perovskite is expected to be the third most abundant phase in the Earth's transition zone and lower mantle, where it may account for up to 25 vol.% of subducted basaltic crust and up to 10 vol.% of a pyrolitic mantle[1,2]. Direct evidence for its existence has recently been reported from analysis of inclusions in superdeep diamonds[10,11]. At 295 K and high pressure ($P$), $CaSiO_3$ perovskite has a tetragonal crystal structure, but undergoes a phase transition to a cubic structure with increasing temperature ($T$), stabilizing the cubic phase along a typical mantle geotherm[6,7,12,13]. It has been inferred that the elastic properties of cubic $CaSiO_3$ perovskite might explain regions of reduced shear-wave velocities in the uppermost lower mantle[6] as well as some of the unique seismic properties of the large low-shear-velocity provinces (LLSVP) that are observed by seismology in the deep lower mantle[7–9].

Although recent works have successfully measured elastic-wave velocities of cubic $CaSiO_3$ perovskite at high pressure and high temperature[6,7], experimental information on its rheology is absent. Previous studies of the deformation behaviours of $CaSiO_3$ are limited to its tetragonal polymorph at room temperature[3,4], owing to experimental difficulties preventing access to mantle-like $P$–$T$ conditions. These works suggest that $CaSiO_3$ perovskite is characterized by a high plastic strength, exceeding that of $MgSiO_3$ bridgmanite, the dominant phase in the Earth's lower mantle. Early computational work, however, predicted that the lattice friction, that is, the Peierls stress, of the ⟨110⟩{1–10} slip system in cubic $CaSiO_3$ perovskite is almost zero[14], which appears incompatible with a very large plastic strength. Theoretical work further suggested that the Peierls stress increases with structural distortions in perovskite-structured materials[15]. The deformation behaviour of cubic $CaSiO_3$ perovskite might thus markedly differ from that of its tetragonal counterpart.

Here we synthesized and deformed cubic $CaSiO_3$ perovskite at 1,150 ± 50 K (Fig. 1) in a recently developed high-pressure and high-temperature apparatus[16] coupled to synchrotron-based radial X-ray diffraction at the Extreme Conditions Beamline, P02.2, at PETRA III, DESY, Hamburg, Germany. High-pressure lattice strains, $Q(hkl)$, were extracted from the recorded diffraction images by fitting the experimental observations using the programme MAUD (see Methods), where $hkl$ refers to the Miller indices of the respective lattice planes. The deviatoric stress $t$ supported by the sample was calculated from the average of measured lattice strains, $\langle Q(hkl)\rangle$, using the identity $t = 6\langle Q(hkl)\rangle G$, where the high-pressure shear modulus, $G$, at 1,150 K was taken from ref. [7]. Texture development was observed in $CaSiO_3$ perovskite throughout the experiment. The observation of texture development, as well as plasticity modelling, shows that plastic deformation occurred in the sample (Extended Data Figs. 3, 4) and measured stresses can thus be treated as approximations for the plastic strength of the sample[17]. The observed texture strength in our high-temperature experiments is slightly higher than in previous experiments at room temperature[3], possibly a result of the lower strength of the sample.

[1]Bayerisches Geoinstitut (BGI), University of Bayreuth, Bayreuth, Germany. [2]University of Utah, Salt Lake City, UT, USA. [3]Deutsches Elektronen-Synchrotron (DESY), Hamburg, Germany. [4]German Research Center for Geosciences (GFZ), Potsdam, Germany. [5]Independent researcher, Bayreuth, Germany. [6]Seismological Laboratory, California Institute of Technology, Pasadena, CA, USA. [7]Present address: Department of Earth Sciences, University of Oxford, Oxford, UK. ✉e-mail: Hauke.Marquardt@earth.ox.ac.uk

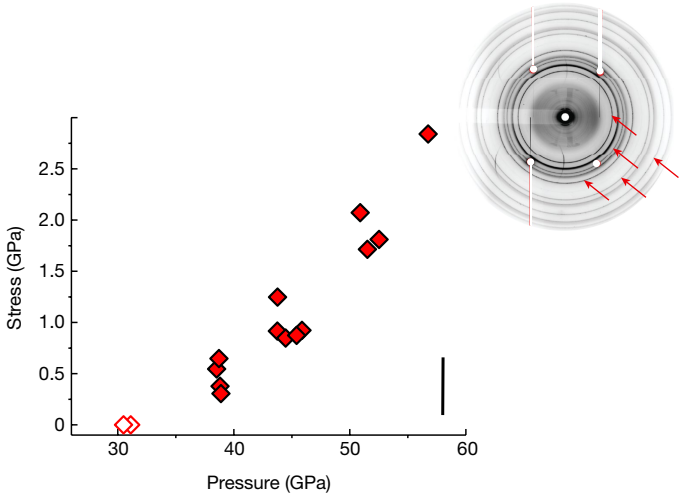


**Fig. 1 | Deviatoric stress measured in cubic $CaSiO_3$ perovskite at lower-mantle pressures and $T$ = 1,150 ± 50 K.** Texture development is observed from 39 GPa (see Methods), indicating plastic flow. Open symbols denote data that have been collected shortly after synthesis and have been excluded from the strength calculation. The size of the experimental errors, propagated from the uncertainties in measured $Q$ values, is indicated by the bar in the lower right corner. The inset shows a typical diffraction pattern collected after in situ high-pressure, high-temperature synthesis of cubic $CaSiO_3$ perovskite in the diamond-anvil cell showing Debye rings of cubic $CaSiO_3$ (denoted by arrows) and platinum (all other rings). Strong XRD contributions related to the diamond-anvils have been masked (white dots/stripes).

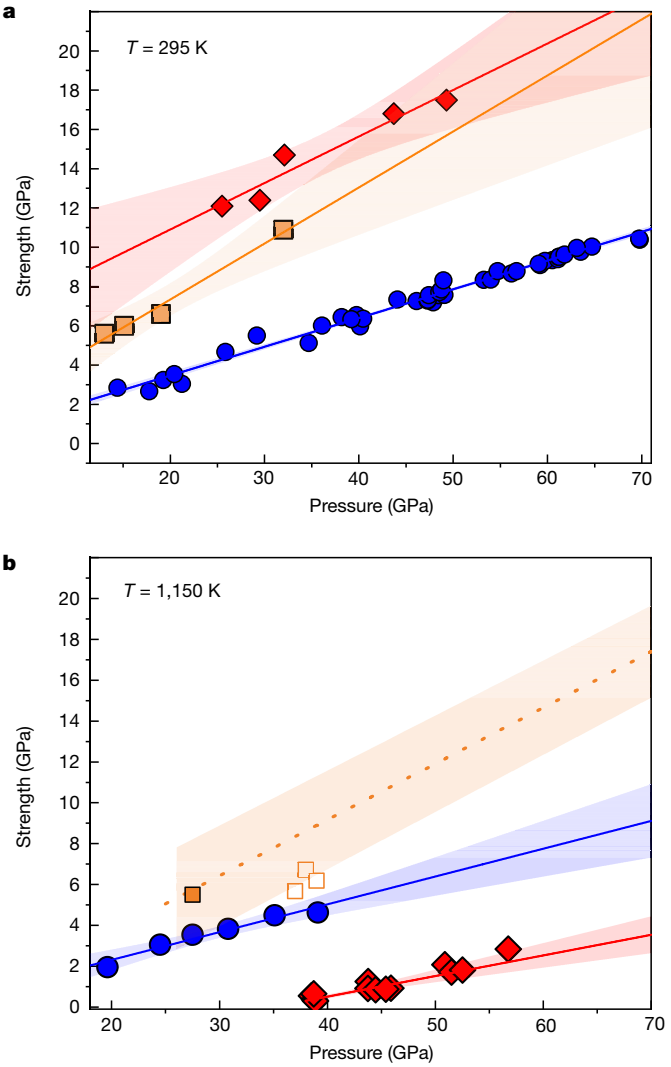


**Fig. 2 | Strength of major lower-mantle phases at high pressures. a**, Strength values measured at room temperature by previous works. Red, (tetragonal) $CaSiO_3$ perovskite[3]; orange, $Mg_{0.9}Fe_{0.1}SiO_3$ bridgmanite[21]; blue, $(Mg_{0.8}Fe_{0.2})O$ ferropericlase[22]. **b**, Here-derived high-temperature strength of cubic $CaSiO_3$ perovskite at lower-mantle pressures (red solid diamonds) compared to the strength of $(Mg_{0.8}Fe_{0.2})O$ measured at 1,150 K (blue solid circles)[18] and the stress measured on bridgmanite deformed as part of a multi-phase assemblage at 1,000 K at comparably low strains, probably representing a lower bound to the high-temperature strength of bridgmanite (open squares)[19]. The solid orange square denotes the strength of bridgmanite at 2,150 K, taken from ref. [20] (the maximum measured stress for bridgmanite in their run 'gamma 25'). Errors reported on the strength values from literature are typically on the order of the symbol sizes (below 1-2 GPa), except for the data point for bridgmanite from ref. [20], where a larger error is reported. Best-fit lines are shown along with their 95% confidence range. Given the limited amount of high-temperature data, the strength of bridgmanite at 1,150 K was derived from the data measured for bridgmanite at 295 K (ref. [21]) by applying two different temperature corrections, represented by the shaded region (see Methods). Even though we acknowledge that this procedure is uncertain, the overlap of our derived range with the available high-temperature data suggest that it provides a reasonable estimate.

In Fig. 2, we compare the here-derived high-temperature strength of cubic $CaSiO_3$ perovskite to previously derived values for (Mg,Fe)O ferropericlase[18] and bridgmanite[19,20], as well as to reported strengths at room temperature[3,21,22]. We note that almost all shown values have been determined by radial X-ray diffraction in a diamond-anvil cell, permitting a direct comparison. Remarkably, cubic $CaSiO_3$ perovskite is characterized by a high-temperature plastic strength that is substantially lower than that reported for bridgmanite and even ferropericlase, which has previously been regarded as the weakest major lower-mantle phase[20,22–24], possibly only rivalled by post-perovskite below approximately 2,500 km depth[25]. Notably, the strength of $CaSiO_3$ measured here at 1,150 K is substantially lower than the strength of bridgmanite previously derived at 2,150 K (at 27.5 GPa)[20].

A particularly interesting observation is the large strength contrast between tetragonal $CaSiO_3$ measured at 295 K (Fig. 2a) and cubic $CaSiO_3$ perovskite at 1,150 K (Fig. 2b). Although strength is expected to decrease with temperature, the here-observed decrease is much larger than expected from a rise in temperature alone as evident by comparison to ferropericlase (Fig. 2). It appears likely that the tetragonal lattice distortion experienced by $CaSiO_3$ perovskite upon temperature decrease leads to an additional increase in strength. This observation is qualitatively consistent with computational work that predicts that Peierls stresses increase with lattice distortions in perovskite-structured materials[15].

We use the here-derived strength values, together with the previous results shown in Fig. 2, to estimate the viscosity contrast between cubic $CaSiO_3$ perovskite, bridgmanite and ferropericlase in the lower mantle. Whereas our measurements have been performed at pressure and temperature conditions typical for the slab's interior at shallow lower-mantle conditions, a major difference between our experiments and deformation in the Earth's mantle is the strain rate and the magnitude of stress. Assuming that the observed rheological behaviour is governed by a dislocation-dominated process as expected for high strain rates in both our experiments and subducted slabs in the Earth's mantle, it can be described by $\dot{\varepsilon} = A\sigma^n$, where $\dot{\varepsilon}$ is the strain rate, $\sigma$ is stress, $n$ is the stress exponent and $A$ is a pre-factor.

We used the identity above, together with the definition of viscosity, $\eta = \sigma/2\dot{\varepsilon}$, to calculate viscosity ratios between the major lower-mantle phases bridgmanite, ferropericlase and $CaSiO_3$ perovskite using the

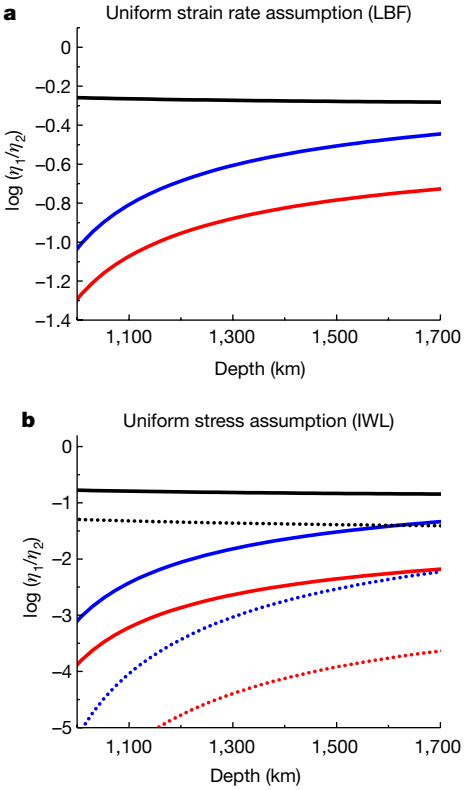


**Fig. 3 | Depth-dependent viscosity contrast between major lower-mantle phases at approximately 1,150 K.** The viscosity contrast is shown for pairs of mantle phases of viscosity $\eta_1$ and $\eta_2$. Red curve, $\eta_{CaSiO3}/\eta_{Bm}$; blue curve, $\eta_{CaSiO3}/\eta_{Fp}$; black curve, $\eta_{Fp}/\eta_{Bm}$. **a**, Viscosity contrast calculated under the assumption that the strain rate is equal in both phases. This assumption represents the stage of initial deformation that is dominated by a load-bearing framework (LBF) of the harder phase. **b**, Viscosity contrast calculated for a uniform stress assumption, representing a scenario of progressed deformation that has led to the development of an interconnected weak layer (IWL) of the weak phase. Calculations have been performed with a stress exponent of $n = 3$ (solid curves) and $n = 5$ (dotted curves).

strength values in Fig. 2b. Initially, we assumed that the strain rates in all experiments were the same ($10^{-4}$ $s^{-1}$)[22] and that samples were deformed by similar processes and hence are described by the same stress exponent (3–5). However, deviations from these assumptions were tested (see Extended Data Table 1). Under these assumptions, the calculated viscosity ratios are independent of the values chosen for mantle stress and strain rate, and only mildly sensitive to the chosen stress exponent (Fig. 3, see also Methods).

Figure 3 shows two endmember scenarios. Figure 3a reflects a situation where the rock deforms as a whole and the strain rate is uniform, a situation that is characteristic for a load-bearing framework (LBF)-type deformation. Figure 3b reflects a situation where strain partitions in the weaker phase and stress is equally distributed between the phases, a situation that is characteristic for an interconnected weak layer (IWL)-type deformation. Cubic $CaSiO_3$ perovskite is always the weakest mantle phase and often shows a viscosity that is several orders of magnitude smaller than that of bridgmanite and ferropericlase. At 1,000-km depths, corresponding to a pressure of about 40 GPa where experimental results for all phases are available, we find cubic $CaSiO_3$ to have a viscosity that is 1.4 to 4 orders of magnitude lower as compared to bridgmanite, and 1 to 3 orders of magnitude lower than ferropericlase (for $n = 3$). The viscosity contrast is particularly pronounced for the IWL scenario, which probably develops in large-strain regions of the mantle. To test the robustness of our findings, we evaluated the effect of assuming different experimental strain rates and stress exponents for bridgmanite, ferropericlase and $CaSiO_3$ perovskite (see Methods). We found that viscosities consistently increased from $CaSiO_3$ perovskite to ferropericlase to bridgmanite for a wide range of model parameters. We note that the calculation of viscosity contrasts by necessity involves several assumptions and relies on poorly constrained parameters, as detailed in Methods; future experimental and theoretical work might aim to better quantify these. The presence of hydrogen in the lower mantle might further affect the rheological behaviour of $CaSiO_3$ perovskite (and bridgmanite), even though a recent study showed that the effect might be small[26].

The presence of weak cubic $CaSiO_3$ perovskite could have wide-ranging consequences for the dynamics of subducting slabs and the interpretation of seismic observations. The formation of $CaSiO_3$ perovskite from majoritic garnet, a comparably hard phase[27], at around 550 km depth in subducted oceanic crust[28] will lead to a substantial weakening of the oceanic crust. Previous works on two-phase deformation of a bridgmanite–ferropericlase assemblage, a proxy for a lower-mantle rock, have predicted that strain starts to partition into the weak ferropericlase that can form an IWL network during deformation, thereby substantially lowering the viscosity of the two-phase assemblage[20,22–24,29]. However, the onset of strain localization largely depends on the viscosity contrast between the phases and the volume fraction of the weak phase[24]. Our results suggest that the viscosity contrast between bridgmanite and cubic $CaSiO_3$ perovskite is substantially larger as compared to that between bridgmanite and ferropericlase. Moreover, the volume fraction of $CaSiO_3$ perovskite in subducted oceanic crust is larger than the ferropericlase fraction in a pyrolitic lower-mantle rock.

Taking this together, we expect strain localization to occur in subducted oceanic crust after the onset of cubic $CaSiO_3$ perovskite formation. $CaSiO_3$ perovskite gradually forms with depths from majoritic garnet and its volume fraction continuously increases between about 550 km and 700 km depth[28]. Deformation of the crust will initially be governed by a LBF of the hard phase(s), which, depending on depth, are majoritic garnet, bridgmanite and stishovite[30]. In this scenario, the effective viscosity contrast can be approximated by a constant strain rate assumption (Fig. 3a). With increasing deformation, strain will start to partition into the weak $CaSiO_3$ phase, leading to rock weakening and initiating a continuous transition towards a deformation scenario where stress is equally distributed between all phases (Fig. 3b). The increase in effective viscosity contrasts between the phases that is caused by this transition will accelerate strain partitioning, further weakening the subducted crust.

We expect cubic $CaSiO_3$ perovskite to form and strain to build up from around 550 km depth, and so we speculate that the strain-weakening effect in subducted oceanic crust will already be sizeable at the time of bridgmanite and ferropericlase formation at around 660 km depth in the surrounding mantle. The weak layer of subducted oceanic crust would thus be sandwiched between comparably hard mantle rocks and could easily be separated from the surrounding mantle by shear forces[31], similar to sediments in the shallower parts of subduction zones. At depths between 660 km and 720 km, basaltic oceanic crust is less dense than surrounding mantle[32], but below about 720 km—after garnet has completely dissolved into perovskite-structured phases—oceanic crust becomes denser than ambient mantle[32,33]. Depending on the depth-dependent buoyancy contrast to the surrounding mantle, low-viscosity oceanic crust could thus segregate and accumulate around 660 km depth[5] or migrate towards the core–mantle boundary, behaving like an 'upside-down plume'. The low viscosity of cubic $CaSiO_3$ perovskite provides an intrinsic mechanism to separate slab materials and to accumulate recycled oceanic crust either at the boundary between the upper and lower mantle or at the core–mantle boundary, where cubic $CaSiO_3$ perovskite may contribute to seismically observed regions of low shear-wave velocities in the uppermost lower mantle[5], as well as in the LLSVPs beneath Africa and the Pacific, as hypothesized

earlier[7–9]. Deep recycling of oceanic crust has further been inferred to contribute to the geochemical diversity observed in ocean island basalts at the surface[34].

The above-mentioned implications require the presence of cubic $CaSiO_3$ perovskite and hence the tetragonal–cubic transition to occur at temperatures below the geotherm[7,12]. If lower-mantle $CaSiO_3$ perovskite contains titanium or aluminium as suggested by the analysis of a diamond inclusion[11], the tetragonal–cubic transition is shifted to higher temperatures[7,12,35], possibly intersecting a cold subduction geotherm[7]. The tetragonal–cubic transition could then lead to sudden changes of rheological properties, which would affect the dynamic behaviour of a subducting slab, possibly leading to slab buckling, delamination or stagnation. The dependence of this dynamic change on the availability of titanium and aluminium could help explain the diverse behaviour of slabs in the lower mantle[36]. Details of the interaction of a weak subducting crust, as indicated by our experiments, with the surrounding mantle should be explored by future geodynamic modelling, as should be the effect of the presence of an Al-bearing phase in subducted oceanic crust that might further complicate slab rheology.

## Online content

Any methods, additional references, Nature Research reporting summaries, source data, extended data, supplementary information, acknowledgements, peer review information; details of author contributions and competing interests; and statements of data and code availability are available at https://doi.org/10.1038/s41586-021-04378-2.


1. Irifune, T. & Tsuchiya, T. Mineralogy of the Earth – phase transitions and mineralogy of the lower mantle. In Treatise on Geophysics. Volume 2: Mineral Physics 1st edn (ed. Schubert, G.) 33–62 (Elsevier, 2007).
2. Hirose, K., Sinmyo, R. & Hernlund, J. Perovskite in Earth's deep interior. *Science* **358**, 734–738 (2017).
3. Miyagi, L. et al. Diamond anvil cell deformation of $CaSiO_3$ perovskite up to 49 GPa. *Phys. Earth Planet. Inter.* **174**, 159–164 (2009).
4. Shieh, S. R., Duffy, T. S. & Shen, G. Elasticity and strength of calcium silicate perovskite at lower mantle pressures. *Phys. Earth Planet. Inter.* **143–144**, 93–105 (2004).
5. Ballmer, M. D., Schmerr, N. C., Nakagawa, T. & Ritsema, J. Compositional mantle layering revealed by slab stagnation at ~1000-km depth. *Sci. Adv.* **1**, e1500815 (2015).
6. Gréaux, S. et al. Sound velocity of $CaSiO_3$ perovskite suggests the presence of basaltic crust in the Earth's lower mantle. *Nature* **565**, 218–221 (2019).
7. Thomson, A. R. et al. Calcium silicate perovskite's acoustic velocities can explain LLSVPs in Earth's lower mantle. *Nature* **572**, 643–647 (2019).
8. Jones, T. D., Maguire, R. R., van Keken, P. E., Ritsema, J. & Koelemeijer, P. Subducted oceanic crust as the origin of seismically slow lower-mantle structures. *Prog. Earth Planet. Sci.* **7**, 17 (2020).
9. Garnero, E. J., McNamara, A. K. & Shim, S.-H. Continent-sized anomalous zones with low seismic velocity at the base of Earth's mantle. *Nat. Geosci.* **9**, 481–489 (2016).
10. Tschauner, O. et al. Discovery of davemaoite, $CaSiO_3$-perovskite, as a mineral from the lower mantle. *Science* **374**, 891–894 (2021).
11. Nestola, F. et al. $CaSiO_3$ perovskite in diamond indicates the recycling of oceanic crust into the lower mantle. *Nature* **555**, 237–241 (2018).
12. Komabayashi, T., Hirose, K., Sata, N., Ohishi, Y. & Dubrovinsky, L. S. Phase transition in $CaSiO_3$ perovskite. *Earth Planet. Sci. Lett.* **260**, 564–569 (2007).
13. Sun, N. et al. Confirming a pyrolitic lower mantle using self-consistent pressure scales and new constraints on $CaSiO_3$ perovskite. *J. Geophys. Res. Solid Earth* **121**, 4876–4894 (2016).
14. Ferré, D., Cordier, P. & Carrez, P. Dislocation modeling in calcium silicate perovskite based on the Peierls–Nabarro model. *Am. Mineral.* **94**, 135–142 (2009).
15. Ferré, D., Carrez, P. & Cordier, P. Peierls dislocation modelling in perovskite ($CaTiO_3$): comparison with tausonite ($SrTiO_3$) and $MgSiO_3$ perovskite. *Phys. Chem. Miner.* **36**, 233–239 (2009).
16. Immoor, J. et al. An improved setup for radial diffraction experiments at high pressures and high temperatures in a resistive graphite-heated diamond anvil cell. *Rev. Sci. Instrum.* **91**, 045121 (2020).
17. Merkel, S. et al. Deformation of polycrystalline MgO at pressures of the lower mantle. *J. Geophys. Res.* **107**, 2271 (2002).
18. Immoor, J. et al. Evidence for {100} ⟨011⟩ slip in ferropericlase in Earth's lower mantle from high-pressure/high-temperature experiments. *Earth Planet. Sci. Lett.* **489**, 251–257 (2018).
19. Couper, S., Speziale, S., Marquardt, H., Liermann, H. P. & Miyagi, L. Does heterogeneous strain act as a control on seismic anisotropy in Earth's lower mantle? *Front. Earth Sci.* **8**, 540449 (2020).
20. Girard, J., Amulele, G., Farla, R., Mohiuddin, A. & Karato, S.-i Shear deformation of bridgmanite and magnesiowüstite aggregates at lower mantle conditions. *Science* **351**, 144–147 (2016).
21. Merkel, S. et al. Deformation of $(Mg_{0.9}Fe_{0.1})SiO_3$pPerovskite aggregates up to 32 GPa. *Earth Planet. Sci. Lett.* **209**, 351–360 (2003).
22. Marquardt, H. & Miyagi, L. Slab stagnation in the shallow lower mantle linked to an increase in mantle viscosity. *Nat. Geosci.* **8**, 311–314 (2015).
23. Yamazaki, D. & Karato, S.-i Some mineral physics constraints on the rheology and geothermal structure of Earth's lower mantle. *Am. Mineral.* **86**, 385–391 (2001).
24. Thielmann, M., Golabek, G. J. & Marquardt, H. Ferropericlase control of lower mantle rheology: impact of phase morphology. *Geochem. Geophys. Geosys.* **21**, e2019GC008688 (2020).
25. Goryaeva, A. M., Carrez, P. & Cordier, P. Low viscosity and high attenuation in $MgSiO_3$ post-perovskite inferred from atomic-scale calculations. *Sci. Rep.* **6**, 34771 (2016).
26. Muir, J. M. R. & Brodholt, J. P. Water distribution in the lower mantle: implications for hydrolytic weakening. *Earth Planet. Sci. Lett.* **484**, 363–369 (2018).
27. Kavner, A., Sinogeikin, S. V., Jeanloz, R. & Bass, J. D. Equation of state and strength of natural majorite. *J. Geophys. Res. Solid Earth* **105**, 5963–5971 (2000).
28. Saikia, A., Frost, D. J. & Rubie, D. C. Splitting of the 520-kilometer seismic discontinuity and chemical heterogeneity in the mantle. *Science* **319**, 1515–1518 (2008).
29. Takeda, Y.-T. Flow in rocks modelled as multiphase continua: application to polymineralic rocks. *J. Struc. Geol.* **20**, 1569–1578 (1998).
30. Hunt, S. A. et al. An experimental investigation of the relative strength of the silica polymorphs quartz, coesite, and stishovite. *Geochem. Geophys. Geosys.* **20**, 1975–1989 (2019).
31. van Keken, P. E., Karato, S. & Yuen, D. A. Rheological control of oceanic crust separation in the transition zone. *Geophys. Res. Lett.* **23**, 1821–1824 (1996).
32. Hirose, K., Fei, Y., Ma, Y. & Mao, H.-K. The fate of subducted basaltic crust in the Earth's lower mantle. *Nature* **397**, 53–56 (1999).
33. Hirose, K., Takafuji, N., Sata, N. & Ohishi, Y. Phase transition and density of subducted MORB crust in the lower mantle. *Earth Planet. Sci. Lett.* **237**, 239–251 (2005).
34. Hofmann, A. W. Mantle geochemistry: the message from oceanic volcanism. *Nature* **385**, 219–229 (1997).
35. Kurashina, T., Hirose, K., Ono, S., Sata, N. & Ohishi, Y. Phase transition in Al-bearing $CaSiO_3$ perovskite: implications for seismic discontinuities in the lower mantle. *Phys. Earth Planet. Inter.* **145**, 67–74 (2004).
36. Fukao, Y. & Obayashi, M. Subducted slabs stagnant above, penetrating through, and trapped below the 660 km discontinuity. *J. Geophys. Res.* **118**, 5920–5938 (2013).

# Methods

### Experimental details

A resistive-heated diamond-anvil cell (DAC), based on a customized Mao–Bell-type DAC and designed for radial X-ray diffraction experiments, was used for the experiments[16]. Diamonds with culet sizes of 300 μm were used, together with a gasket made of an amorphous boron epoxy mixture that was inserted in a Kapton foil. A resistive heater that surrounds the diamond tips was made of two thin flexible graphite layers that are in tight contact with the diamond anvils. A beam path was carved into the graphite sheets[16,37] to allow X-rays to pass through the heater . The entire DAC was positioned inside a vacuum chamber designed at the Extreme Condition Beamline (ECB, P02.2) at PETRA III of the Deutsches Elektronen-Synchrotron (DESY)[16,38]. A vacuum of better than $10^{-4}$ mbar was maintained during the experiment to avoid oxidation of the cell and diamonds, while the outside of the vacuum chamber was kept at low temperatures by a water-cooling system[16,38]. The starting material was finely ground powder of $CaSiO_3$ wollastonite, containing minor amounts of Al, Fe and Ti (<0.2 at.% according to electron microprobe analysis), mixed with a small amount of fine-powdered platinum to determine the experimental pressure, using previously published thermal equation-of-state parameters[39]. The sample was heated at a pressure of ~30 GPa until the appearance of new diffraction rings indicated the formation of $CaSiO_3$ perovskite (Fig. 1). Temperature was increased slowly (hours) to allow the system to equilibrate and maintain the vacuum. Pressure was then increased at a constant temperature of 1,150 ± 50 K, leading to deformation of the sample. Temperature was determined as the average of the measurement of two thermocouples placed between the heater and below the gasket[16], with the given uncertainty reflecting the difference between the two measurements. Pressure was increased remotely using a gas-membrane system and diffraction images were taken after the pressure stabilized. X-ray diffraction experiments were performed at the Extreme Conditions Beamline (ECB) P02.2 at PETRA III at DESY[38]. X-rays (wavelength of 0.4871 Å) were focused to 8 (horizontal) × 3 (vertical) μm² (full width at half maximum). The diffraction images were recorded on a Perkin Elmer XRD 1621 flat panel detector (sample–detector distance of 410.4 mm), sliced using the Fit2d software[40] and analysed using the software package MAUD[41] (Extended Data Fig. 1). The "radial diffraction in the DAC" model[42] was used to fit lattice strains (110, 111, 200, 211 reflections) in $CaSiO_3$ perovskite. The E-WIMW model—which is similar to the WIMV model[43], but allows for incomplete and arbitrary pole figure coverage—was used to fit textures. Cylindrical symmetry was imposed. The orientation distribution function (ODF) was exported to BEARTEX[44] to plot inverse pole figures. Derived lattice strains and texture evolution are shown in Extended Data Figs. 2, 3. A clear texture development is observed throughout the experiment, where texture strength increased from 1.5 multiples of random distribution (mrd) after synthesis to about 1.75 mrd at the highest pressures. It is important to note that both the sample's strength and texture are derived from the same set of grains sampled by the X-rays. It is therefore not possible by experimental design that some highly stressed grains that cause texture development are missing from our strength measurement.

### Visco-plastic self-consistent modelling of texture development

We performed visco-plastic self-consistent (VPSC) simulations[45] to model slip system activities and to determine the amount of plastic strain required to reproduce the experimentally measured increase of texture strength (Extended Data Fig. 4). Simulations were performed using VPSC version 6 with a tangent approximation for the inclusion matrix interaction. The starting texture was discretized into 3,000 grains from the experimentally measured ODF at 31.1 GPa. This was then used as the starting texture for plasticity simulations. Different amounts of strain were applied in the simulation until the texture strength measured at 52.2 GPa was reproduced by the model. The best-fit model required 20% plastic strain with dominant 110 slip (79% of total strain is on 110).

### Modelling of the strength of bridgmanite at 1,150 K and lower-mantle pressures

In absence of direct measurements of the plastic strength of single-phase bridgmanite at relevant pressures and high temperatures, we applied a temperature correction to 295-K DAC experiments[21]. We used the average value of two different approaches, where (1) the effect of temperature on the strength of bridgmanite is assumed to be the same as that measured for ferropericlase, and (2) the 295-K results were shifted to lower strength values to match those measured for bridgmanite deformed in a DAC within a multi-phase assemblage[19].

### Modelling of the viscosity contrast between lower-mantle phases

We used our experimental data to calculate viscosity contrasts between major lower-mantle phases using the identities:

$$\dot{\varepsilon} = A\sigma^n \tag{1}$$

and

$$\eta = \sigma/2\dot{\varepsilon} \tag{2}$$

Here $\eta$ is viscosity, $\dot{\varepsilon}$ is the strain rate, $\sigma$ is stress, $n$ is the stress exponent and $A$ is a pre-factor.

The above relations can be combined to calculate the viscosity contrast between any two phases (denoted by subscripts) for either a uniform stress or uniform strain rate scenario, according to:

$$\frac{\eta_1}{\eta_2} = \frac{\dot{\varepsilon}_2 \sigma_1^{n_1}}{\dot{\varepsilon}_1 \sigma_2^{n_2}} \sigma_g^{(n_2 - n_1)} \text{(for uniform geophysical stress, } \sigma_g) \tag{3}$$

$$\frac{\eta_1}{\eta_2} = \frac{A_2^{\left(\frac{1}{n_2}\right)}}{A_1^{\left(\frac{1}{n_1}\right)}} \dot{\varepsilon}_g^{\left(\frac{1}{n_1} - \frac{1}{n_2}\right)} \text{(for uniform geophysical strain rate, } \dot{\varepsilon}_g) \tag{4}$$

Under the assumption that the strain rates in all experiments were the same and that samples deformed by similar processes and are hence described by the same stress exponent $n$, the above equations can be simplified to:

$$\frac{\eta_1}{\eta_2} = \left(\frac{\sigma_1}{\sigma_2}\right)^n \text{(for uniform geophysical stress)} \tag{5}$$

$$\frac{\eta_1}{\eta_2} = \frac{\sigma_1}{\sigma_2} \text{(for uniform geophysical strain rate)} \tag{6}$$

To test the effect of this simplification on the here-derived viscosity contrasts (Fig. 3), we used equations (3), (4) to test the effect of different stress exponents for the three mantle minerals and differences in experimental strain rates over a relevant range. The results are summarized in Extended Data Table 1. We find that cubic $CaSiO_3$ consistently shows a lower viscosity than both bridgmanite and ferropericlase, often by several orders of magnitude. It shows a particularly low viscosity in our uniform stress models.

## Data availability

Raw data were generated at the Deutsches Elektronen-Synchrotron (DESY) and are available at https://doi.org/10.6084/m9.figshare.17287361. All derived data supporting the findings of this study are available within the article and the Extended Data. Source data for Figs. 2, 3 and Extended Data Fig. 2 are provided with the paper.

37. Liermann, H.-P. et al. Experimental method for in situ determination of material textures at simultaneous high pressure and high temperature by means of radial diffraction in the diamond anvil cell. *Rev. Sci. Instrum.* **80**, 104501 (2009).
38. Liermann, H.-P. et al. The Extreme Conditions Beamline P02.2 and the Extreme Conditions Science Infrastructure at PETRA III. *J. Synchr. Rad.* **22**, 908–924 (2015).
39. Fei, Y. et al. Toward an internally consistent pressure scale. *Proc. Natl Acad. Sci.* **104**, 9182–9186 (2007).
40. Hammersley, A. P., Svensson, S. O., Hanfland, M., Fitch, A. N. & Hausermann, D. Two-dimensional detector software: from real detector to idealised image or two-theta scan. *High Press. Res.* **14**, 235–248 (1996).
41. Lutterotti, L., Matthies, S., Wenk, H.-R., Schultz, A. S. & Richardson, J. W. Jr Combined texture and structure analysis of deformed limestone from time-of-flight neutron diffraction spectra. *J. Appl. Phys.* **81**, 594–600 (1997).
42. Singh, A. K., Balasingh, C., Mao, H.-K., Hemley, R. J. & Shu, J. Analysis of lattice strains measured under nonhydrostatic pressure. *J. Appl. Phys.* **83**, 7567–7575 (1998).
43. Matthies, S. & Vinel, G. W. On the reproduction of the orientation distribution function of texturized samples from reduced pole figures using the conception of a conditional ghost correction. *Phys. Status Solidi B* **112**, K111–K114 (1982).
44. Wenk, H.-R., Matthies, S., Donovan, J. & Chateigner, D. BEARTEX: a Windows-based program system for quantitative texture analysis. *J. Appl. Crystallogr.* **31**, 262–269 (1998).
45. Lebensohn, R. A. & Tomé, C. N. A self-consistent anisotropic approach for the simulation of plastic deformation and texture development of polycrystals: application to zirconium alloys. *Acta Metall. Mater.* **41**, 2611–2624 (1993).

**Acknowledgements** We acknowledge technical assistance by A. Ehnes and I. Schwark. We thank A. R. Thomson for providing a table with the high-temperature shear modulus of $CaSiO_3$ perovskite. This research was supported through the German Science Foundation (grants MA4534/3-1 and MA4534/4-1) as well the European Union's Horizon 2020 research and innovation programme (ERC grant 864877). H.M. acknowledges support from the Bavarian Academy of Sciences. L..M acknowledges support from the NSF (EAR-1654687) and US Department of Energy National Nuclear Security Administration through the Chicago-DOE Alliance Center (DE- NA0003975).

**Author contributions** H.M., H.-P.L., L.M. and S.S. designed the research. J.I. prepared the experiments. All authors contributed to the synchrotron experiments. J.I. and L.M. analysed the data. H.M. performed the modelling. H.M. wrote the initial draft of the manuscript. All authors contributed to the final writing of the manuscript.

**Competing interests** The authors declare no competing interest.

**Additional information**

**Supplementary information** The online version contains supplementary material available at https://doi.org/10.1038/s41586-021-04378-2.

**Correspondence and requests for materials** should be addressed to H. Marquardt.

**Peer review information** *Nature* thanks Patrick Cordier and the other, anonymous, reviewer(s) for their contribution to the peer review of this work.

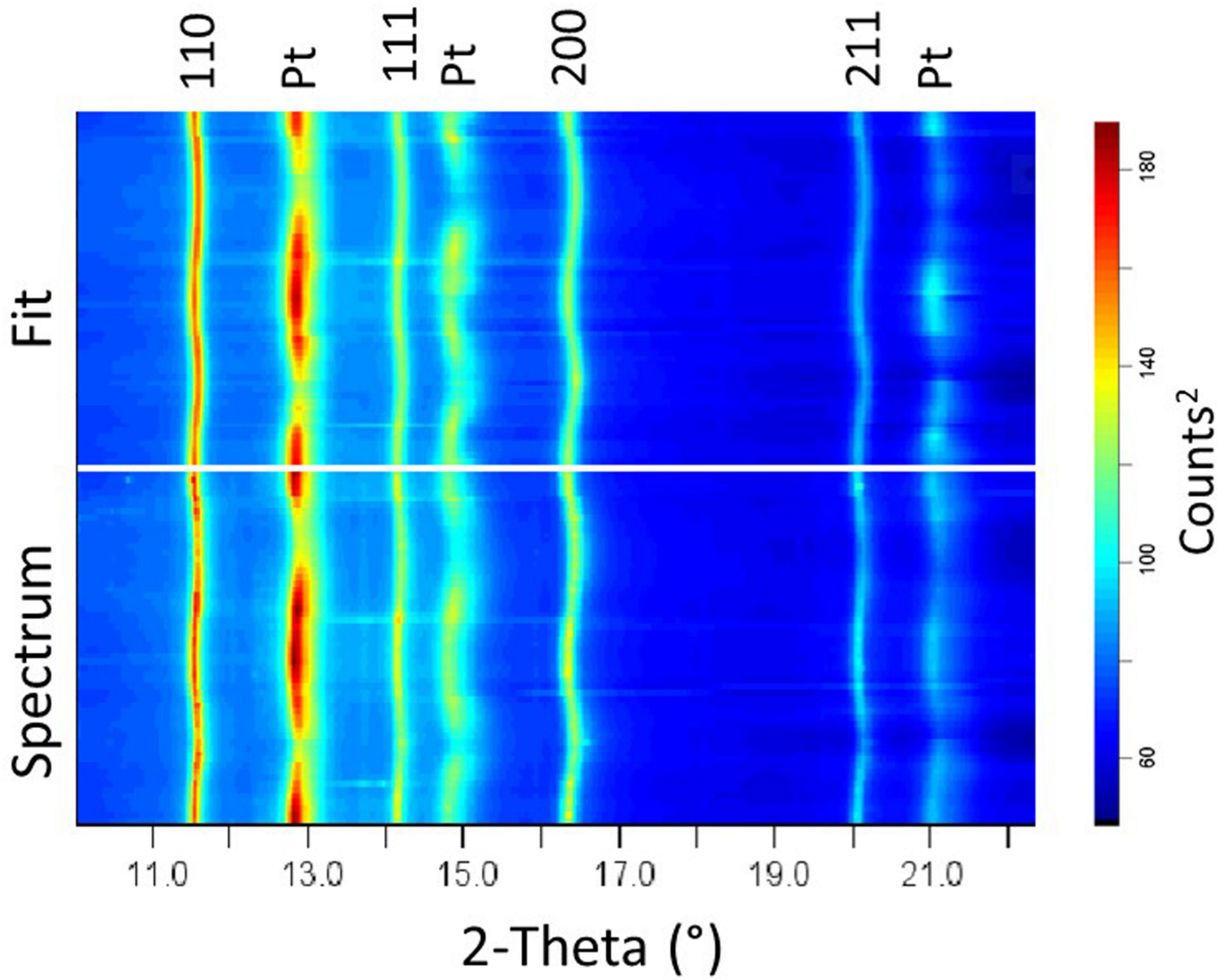


**Extended Data Fig. 1 | Unrolled diffraction image.** Data were collected at 52.5 GPa and 1,150 ± 50 K (bottom) along with the best-fit model (top). The curvature is a measure of lattice strains and was used to calculate the strength of $CaSiO_3$ perovskite.

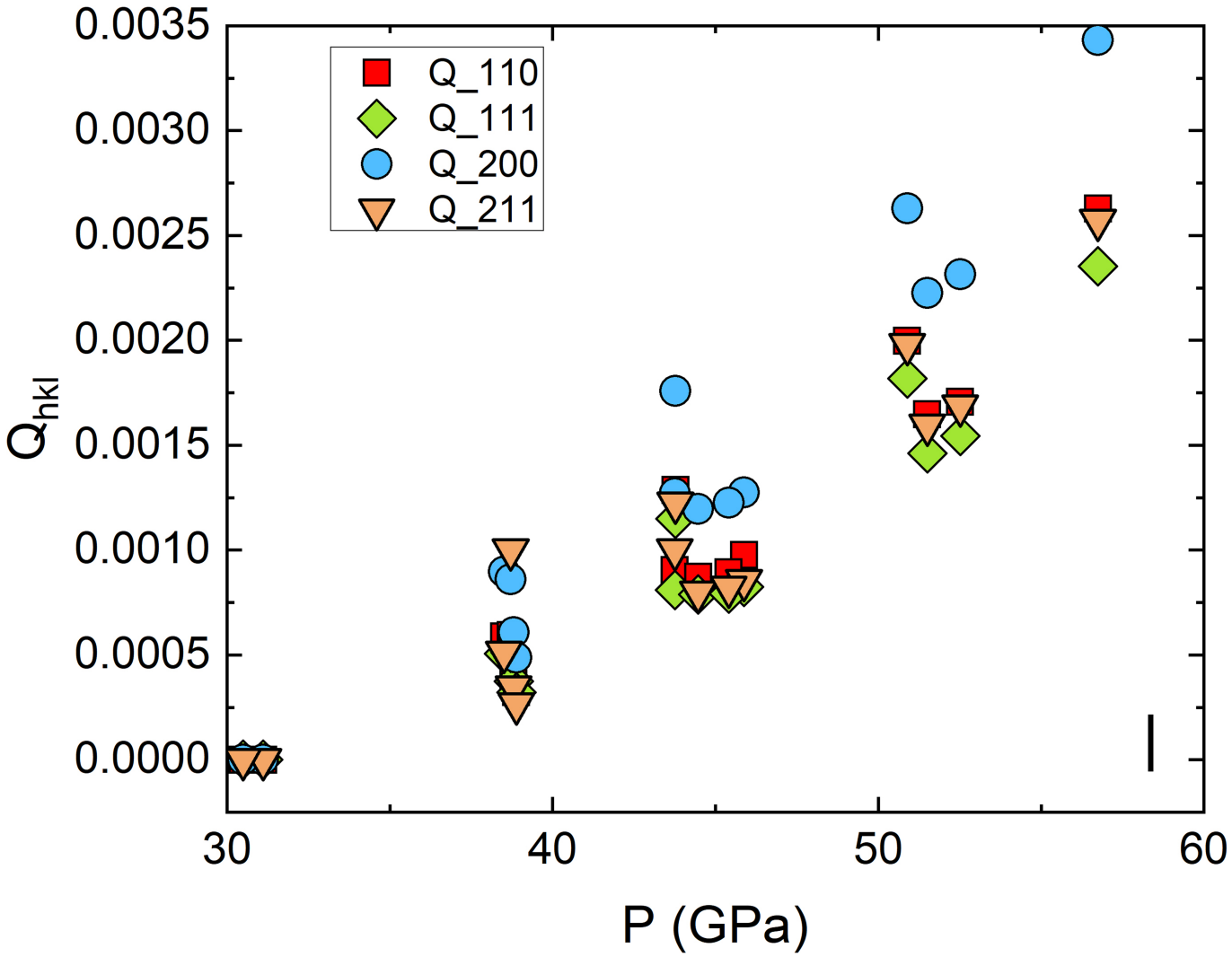


**Extended Data Fig. 2 | Experimentally derived lattice strains of cubic $CaSiO_3$ at a temperature of 1,150 ± 50 K.** The error of the derived lattice strains is similar to the symbol sizes, as shown in the lower right corner.

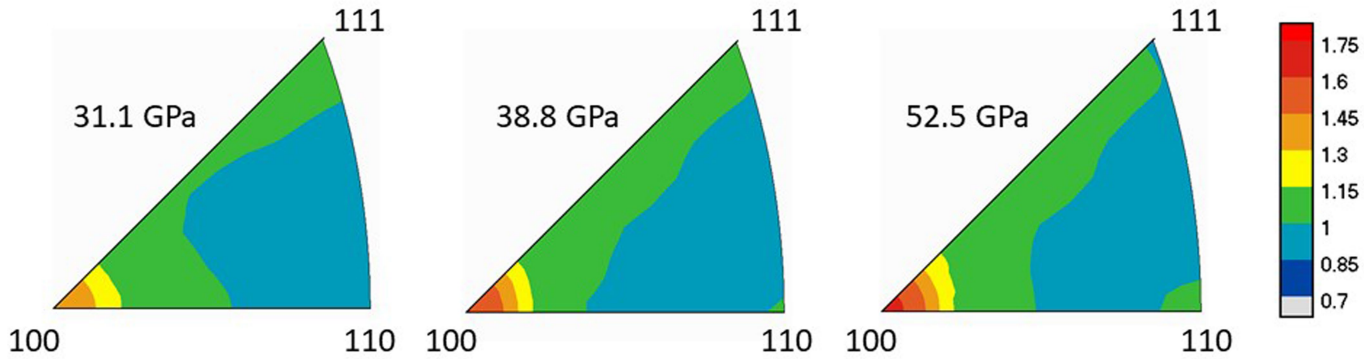


**Extended Data Fig. 3 | Texture development observed in experiments.** Texture strength is indicated by the colours. 100 texture increases with pressure throughout the experiment, increasing from about 1.5 mrd to 1.75 mrd, indicating plastic flow.

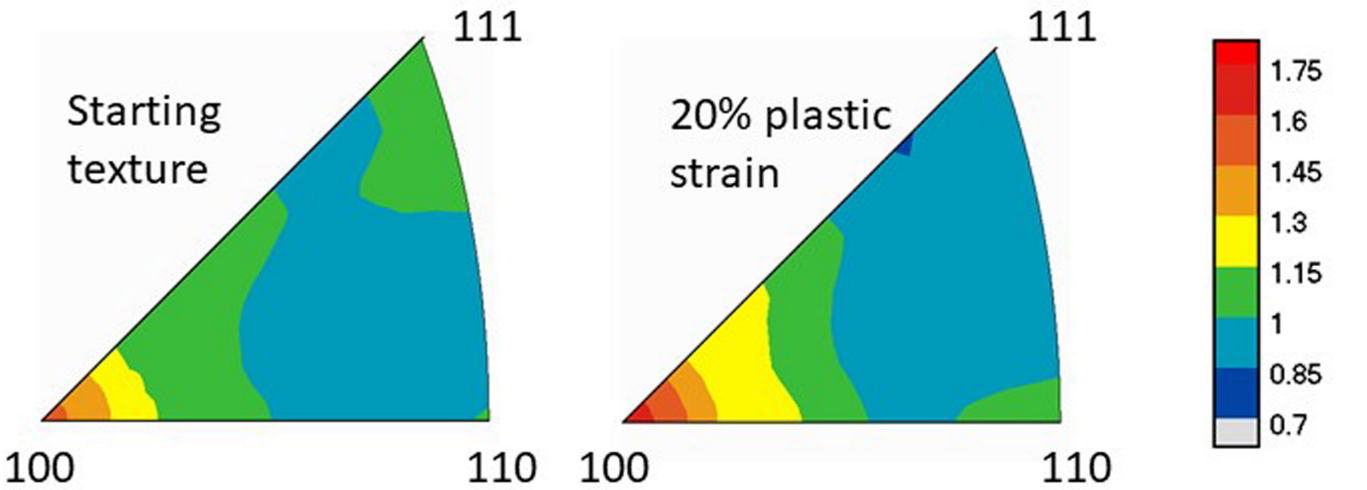


**Extended Data Fig. 4 | VPSC modelling of texture development.** The measured experimental texture after sample synthesis was used as starting texture. 20% of plastic strain leads to a texture strength comparable to that measured at 52.2 GPa (see Extended Data Fig. 3).

**Extended Data Table 1 | Viscosity contrast between $CaSiO_3$ perovskite and bridgmanite (left) or ferropericlase (right)**

| $CaSiO_3$ perovskite / bridgmanite | | | | $CaSiO_3$ perovskite / ferropericlase | | | |
|---|---|---|---|---|---|---|---|
| $n_{Bm}$ | $\dot{\varepsilon}_{Bm}$ ($s^{-1}$) | $LOG(\eta_{CaSiO3}/\eta_{Bm})$ | | $n_{Fp}$ | $\dot{\varepsilon}_{Fp}$ ($s^{-1}$) | $LOG(\eta_{CaSiO3}/\eta_{Fp})$ | |
| | | $\sigma_g$ = constant | $\dot{\varepsilon}_g$ = constant | | | $\sigma_g$ = constant | $\dot{\varepsilon}_g$= constant |
| 3 | $10^{-3} – 10^{-5}$ | -5.9 to -3.9 | -0.1 to -0.7 | 3 | $10^{-3} – 10^{-5}$ | -5.1 to -3.1 | -0.5 to 0.2 |
| 4 | $10^{-3} – 10^{-5}$ | -5.8 to -3.8 | -1.5 to -1.0 | 4 | $10^{-3} – 10^{-5}$ | -4.8 to -2.8 | -1.2 to -0.7 |
| 5 | $10^{-3} – 10^{-5}$ | -5.8 to -3.8 | -1.9 to -1.5 | 5 | $10^{-3} – 10^{-5}$ | -4.5 to -2.5 | -1.7 to -1.3 |

Contrast is calculated from strength values at 40 GPa and ~1,150 K (see Fig. 2b). The effect of varying the stress exponent and experimental strain rate on calculated viscosity contrasts was tested. In calculating the values in the table, we assumed a stress exponent of 4 and an experimental strain rate of $10^{-4}$ $s^{-1}$ for $CaSiO_3$. We further fixed the mantle stress to 10 MPa and the mantle strain rate to $10^{-14}$ $s^{-1}$ for calculations at uniform stress and strain rate, respectively.